Origin of voltage decay in high-capacity layered oxide electrodes

M. Sathiya, Artem M. Abakumov, Dominique Foix, G. Rousse, G Vantendeloo, Danielle Gonbeau, C. P. Laisa, Marie-Liesse Doublet, K. Ramesha, A. Prakash, et al.

Origin of voltage decay in high-capacity layered oxide electrodes

Reference:

Sathiya M., Abakumov Artem M., Foix D., van Tendeloo Gustaaf, et al..- Origin of voltage decay in high-capacity layered oxide electrodes

Nature materials - ISSN 1476-1122 - (2014), p. 1-9

DOI: http://dx.doi.org/doi:10.1038/nmat4137

Handle: http://hdl.handle.net/10067/1210020151162165141

Origin of voltage decay in high-capacity layered oxide electrodes

M. Sathiya[1,2,3], A. M. Abakumov[4], D. Foix[3,5,6], G. Rousse[1,6,7], K. Ramesha[8], D. Gonbeau[3,5,6], M. Saubanère[3,6,9], M. L. Doublet[3,6,9], H. Vezin[10], C. P. Laisa[8], A. S. Prakash[1,8], G. VanTendeloo[4] and J-M. Tarascon[1,3,6]*

Although Li-rich layered oxides ($Li_{1+x}Ni_yCo_zMn_{1-x-y}O_2$, >250 mAh g^{-1}) are attractive electrode materials providing energy densities more than 15% higher than today's commercial Li-ion cells, they suffer from voltage decay on cycling. To elucidate the origin of this phenomenon, we employ chemical substitution in structurally related Li_2RuO_3 compounds. Li-rich layered $Li_2Ru_{1-y}Ti_yO_3$ phases with capacities of ~240 mAh g^{-1} exhibit the characteristic voltage decay on cycling. A combination of transmission electron microscopy and X-ray photoelectron spectroscopy studies reveals that the migration of cations between metal layers and Li layers is a congenital feature of the charge–discharge process that increases the trapping of metal ions in interstitial tetrahedral sites. A correlation between these trapped ions and the voltage decay is established by expanding the study to both $Li_2Ru_{1-y}Sn_yO_3$ and Li_2RuO_3; the slowest decay occurs for the cations with the largest ionic radii. This effect is robust, and the finding provides insights into new chemistry to be explored for developing high-capacity layered electrodes that evade voltage decay.

Lithium-ion battery technology, having the highest gravimetric and volumetric energy densities of commercialized batteries, has conquered the portable electronics market[1,2]. Moreover, it is the battery of choice for powering electric vehicles and has great potential for grid energy storage[3]. Success in these fields will depend on our ability to further increase their energy density[4] to ensure longer cruising autonomy for electric vehicle and lower cost (per kilowatt-hour) to compete with pumped hydroelectric storage for grid applications. To reach such targets, current research mainly focuses on the synthesis of new Fe-based poly-anionic compounds[5,6] and improving the layered oxides used at present[7], the latter being the topic of this paper.

Layered oxides of general formula $LiNi_{1/3}Co_{1/3}Mn_{1/3}O_2$ (NMC) exhibit the highest capacity (≈200 mAh g^{-1}) of any positive-electrode materials used at present[8]. The crystal structure of these materials can be considered as an ordered rock-salt derivative, where octahedrally coordinated Li and transition-metal cations ideally form alternating layers confined to the (111) planes of cubic oxygen close packing[9]. By modifying the chemical composition through substituting M with Li in the metal layers, Thackeray's and Dahn's groups have fabricated materials, termed as Li-rich layered oxides or Li-rich NMC ($Li_{1+x}Ni_yCo_zMn_{1-x-y-z}O_2$), exhibiting reversible capacities exceeding 250 mAh g^{-1} (refs 10,11).The extra capacity was recently shown by complementary X-ray photoelectron spectroscopy (XPS) and electron paramagnetic resonance (EPR) experiments to be nested in the contribution of reversible anionic ($O^{2-} \rightarrow O_2^{2-}$) redox processes to the overall material capacity[12,13]. Nevertheless, it remains that these materials have poor electrode kinetics and undergo large voltage decays (that is, change in slope of the characteristic voltage–composition curves) on cycling, both of which are plaguing their implementation in practical cells[14–16]. Present scenarios, although not fully conclusive, tend to relate this voltage decay to structural effects and more specifically to the formation of spinel-like domains[17–23]. We recently found that the replacement of Mn^{4+} in $Li_2Ru_{1-y}Mn_yO_3$ by the larger and less electropositive cation Sn^{4+} reduces voltage fading[12,24]. To assess the importance of substituent's chemical–physical characteristics on the voltage fade on cycling, we herein extend our work to the study of $Li_2Ru_{1-y}Ti_yO_3$. The Ti^{4+} (d^0) substitution was selected owing to its zero crystal field splitting, similar to d^{10} Sn^{4+}, its smaller size (0.60 Å) and its presumed ability to show accelerated cation migration[25,26] for direct visualization of migration paths.

Members of the $Li_2Ru_{1-y}Ti_yO_3$ series were prepared by thoroughly mixing stoichiometric amounts of RuO_2, TiO_2 and Li_2CO_3 and annealing at 800 °C for 24 h. The resulting single-phase samples form a complete solid solution, demonstrated by the continuous variation of lattice parameters as a function of Ti content (Supplementary Fig. 1). The crystal structure is monoclinic with an atomic distribution corresponding to the Li_2RuO_3 model with some Ru^{4+} (ionic size 0.62 Å) being substituted by Ti^{4+} (ionic size 0.60 Å).

For concision, our study focuses mainly on $Li_2Ru_{0.75}Ti_{0.25}O_3$. A combination of Rietveld refinement from powder X-ray diffraction (XRD) data (Fig. 1a), electron diffraction (Supplementary Fig. 2) and high-angle annular dark-field scanning transmission electron microscopy (HAADF-STEM) imaging (Supplementary Fig. 3) reveals that its structure can be viewed (Fig. 1a, inset) as stacking of Li_3 layers and LiM_2 layers (M = Ru, Ti) along the c axis. In $Li_2Ru_{0.75}Ti_{0.25}O_3$, the Li and (Ru, Ti) cations demonstrate perfect honeycomb-like ordering within the LiM_2 layers; no cation inter-

[1]FRE 3677 'Chimie du Solide et de l'Energie', Collège de France, 11, Place Marcelin Berthelot, 75231 Paris, France, [2]LRCS, CNRS UMR 7314, Université de Picardie Jules Verne, 80039 Amiens, France, [3]ALISTORE-European Research Institute, 80039 Amiens, France, [4]EMAT, University of Antwerp, Groenenborgerlaan 171, B-2020 Antwerp, Belgium, [5]IPREM/ECP (UMR 5254), University of Pau, 2 av. Pierre Angot, 64053 Pau Cedex 9, France, [6]Réseau sur le Stockage Electrochimique de l'Energie (RS2E), FR CNRS 3459, France, [7]Sorbonne Universités UPMC Univ Paris 06, 4 place Jussieu, 75252 Paris Cedex 05, France, [8]CSIR- CECRI- Chennai Centre, CSIR Campus, Taramani, Chennai-600 113, India, [9]Institut Charles Gerhardt, CNRS UMR5253, Université Montpellier 2, 34 095 Montpellier, France, [10]Univ. Lille Nord de France, CNRS, UMR 8516 – LASIR, Univ. Lille 1, F-59655 Villeneuve d'Ascq, France.
*e-mail: jean-marie.tarascon@u-picardie.fr

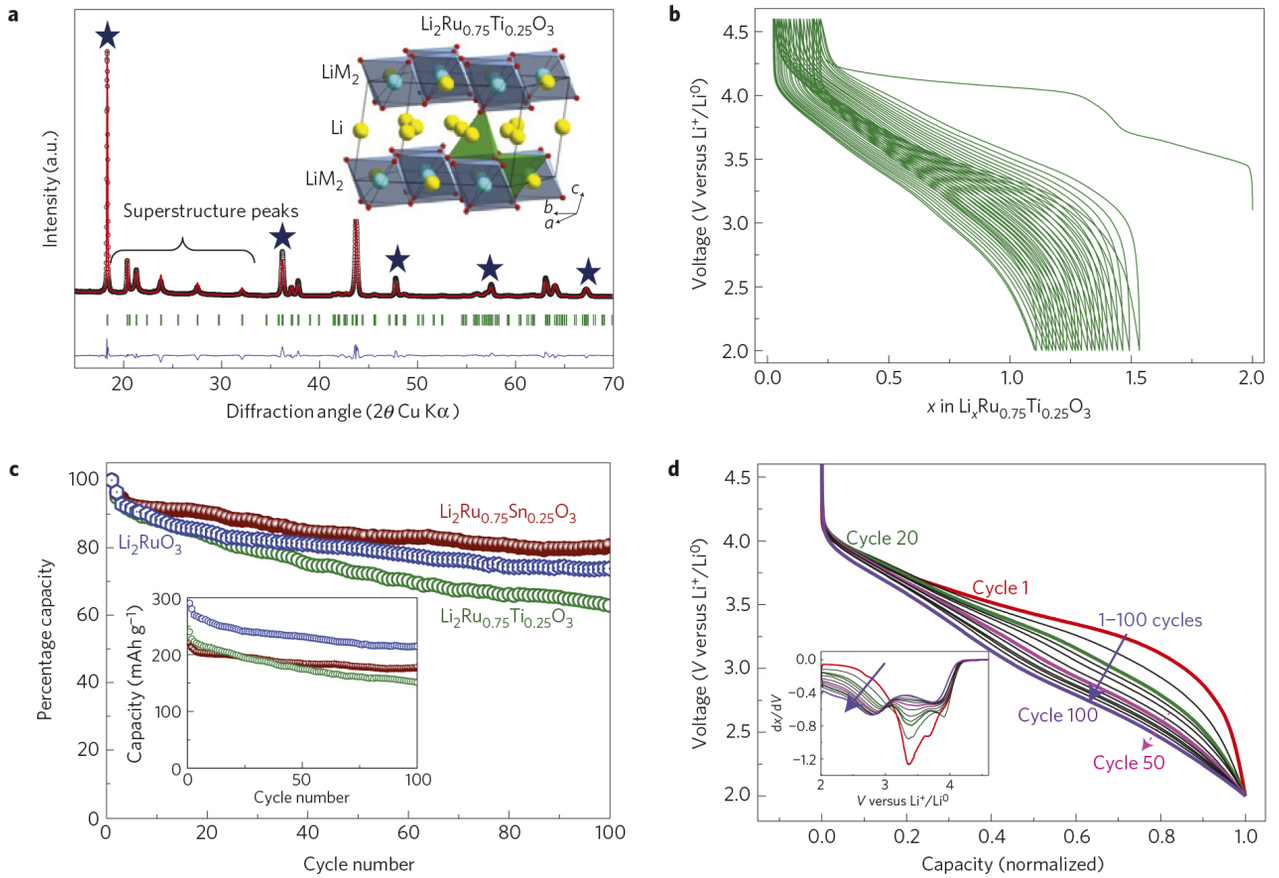

Figure 1 | Structural and electrochemical aspects of $Li_2Ru_{0.75}Ti_{0.25}O_3$. a, Powder XRD pattern (black points) and the Rietveld fit (red lines) for $Li_2Ru_{0.75}Ti_{0.25}O_3$; refinement was carried out using the monoclinic $C2/m$ space group (lattice parameters: $a = 5.037(7)$ Å, $b = 8.717(1)$ Å, $c = 5.126(6)$ Å and $\beta = 109.137(3)°$). Bragg positions are indicated as green vertical tick marks, and the blue line is the difference between the observed and calculated patterns. $R_{Bragg} = 7.88\%$. The peaks marked by stars are the reflections originating from the difference in scattering density between octahedral positions in the Li_3 and LiM_2 layers (interlayer ordering) and can serve as a mean to weigh the interlayer mixing, that is, the amount of transition-metal atoms (Ru/Ti) moving from the octahedral sites of the LiM_2 layers (denoted Oc_{LiM_2}) to the octahedral sites of the Li layers (denoted Oc_{Li_3}). The inset shows the structure of $Li_2Ru_{0.75}Ti_{0.25}O_3$ with stacking of LiM_2 (M = Ru, Ti) and Li_3 layers; Li is yellow, Ru/Ti is blue, possible tetrahedral sites for the occupation of metal ions are shown by green (in the Li_3 and LiM_2 layer) tetrahedra. **b**, Voltage versus composition profile for $Li_2Ru_{0.75}Ti_{0.25}O_3$ versus lithium as deduced from galvanostatic cycling at a 0.2 C rate. **c**, Percentage capacity retention plot of $Li_2Ru_{0.75}Ti_{0.25}O_3$ in comparison with that of Li_2RuO_3 and $Li_2Ru_{0.75}Sn_{0.25}O_3$; the as-measured capacities are presented in the inset. **d**, From cycle 1 to 100, the galvanostatic discharge profile of $Li_2Ru_{0.75}Ti_{0.25}O_3$ versus Li in the 2–4.6 V potential region; every tenth cycle is shown and the capacity values were normalized such that the maximum capacity in each cycle is taken as unity (240 and 151 mAh g^{-1} is taken as unity for the first and hundredth cycles respectively). The inset shows the derivative plot of the same and the evolution of the new redox process at less than 3 V is marked by blue arrow.

mixing between the Li_3 and LiM_2 layers was observed. Thus, two types of cation ordering coexist in the material. The interlayer ordering between the Li_3 and LiM_2 layer drives the structure from the cubic rock salt $Fm\bar{3}m$ aristotype towards an $R\bar{3}m$ sublattice, whereas the honeycomb intralayer ordering decreases the symmetry even further to monoclinic $C2/m$. Stacking faults are therefore abundant (Supplementary Fig. 3) because of lateral shifts and/or 60° rotations of the LiM_2 layers.

The voltage–composition trace for a $Li_2Ru_{1-y}Ti_yO_3$ electrode ($y = 0.25$) shows the feasibility to remove 1.8 Li via two plateaux, of which 1.5 Li can be reinserted via an S-type discharge curve (Fig. 1b). This leads to a reversible capacity of nearly 240 mAh g^{-1} that decreases with increasing y and reaches 110 mAh g^{-1} for $y = 0.75$ (Supplementary Fig. 4).

A common feature of all members of the $Li_2Ru_{1-y}Ti_yO_3$ solid solution series is the large first-cycle irreversibility that increases by increasing the cutoff potential (Supplementary Fig. 5). Such irreversibility may occur partly owing to electrolyte oxidation but is mainly caused by irreversible loss of oxygen from the material[24,27,28] as confirmed by *in situ* gas and pressure analysis, with the onset of an O_2 loss at 4.1 V that then increases continuously as the charging voltage proceeds to 4.5 V (not shown here). Last, similar to all Li-rich NMC or $Li_2Ru_{1-y}M_yO_3$ (M = Mn, Sn) phases, the first charge voltage trace differs from the first discharge trace, suggesting the contribution of a reversible anionic ($O^{2-} \rightarrow O_2^{2-}$) redox process to the overall capacity of $Li_2Ru_{1-y}Ti_yO_3$ samples. However, a minor difference from the Mn- and Sn-based layered electrodes[12,24] is the amplitude of the first-charge 3.7 V plateau for $Li_2Ru_{1-y}Ti_yO_3$, which no longer equals the initial amount of Ru. This suggests another redox process in competition with the $Ru^{4+} \rightarrow Ru^{5+}$ process, as is discussed later.

Long cycling tests performed on Li/$Li_2Ru_{0.75}Ti_{0.25}O_3$ cells (Fig. 1c) were compared to those of Li/$Li_2Ru_{0.75}Sn_{0.25}O_3$ and un-substituted Li_2RuO_3 cells cycled under various cycling rates between 2 V and 4.6 V. All samples exhibit initial capacities exceeding 200 mAh g^{-1} (inset of Fig. 1c) with the Sn- and Ti-based samples showing the highest and lowest capacity retention, respectively (90% versus 62% after 100 cycles). This trend is preserved irrespective of the cycling rate (data not shown here).

In addition, the normalized discharge voltage traces for a Li/$Li_2Ru_{0.75}Ti_{0.25}O_3$ cell show that the voltage decays by nearly 500 mV between the first and hundredth cycle (Fig. 1d). This voltage

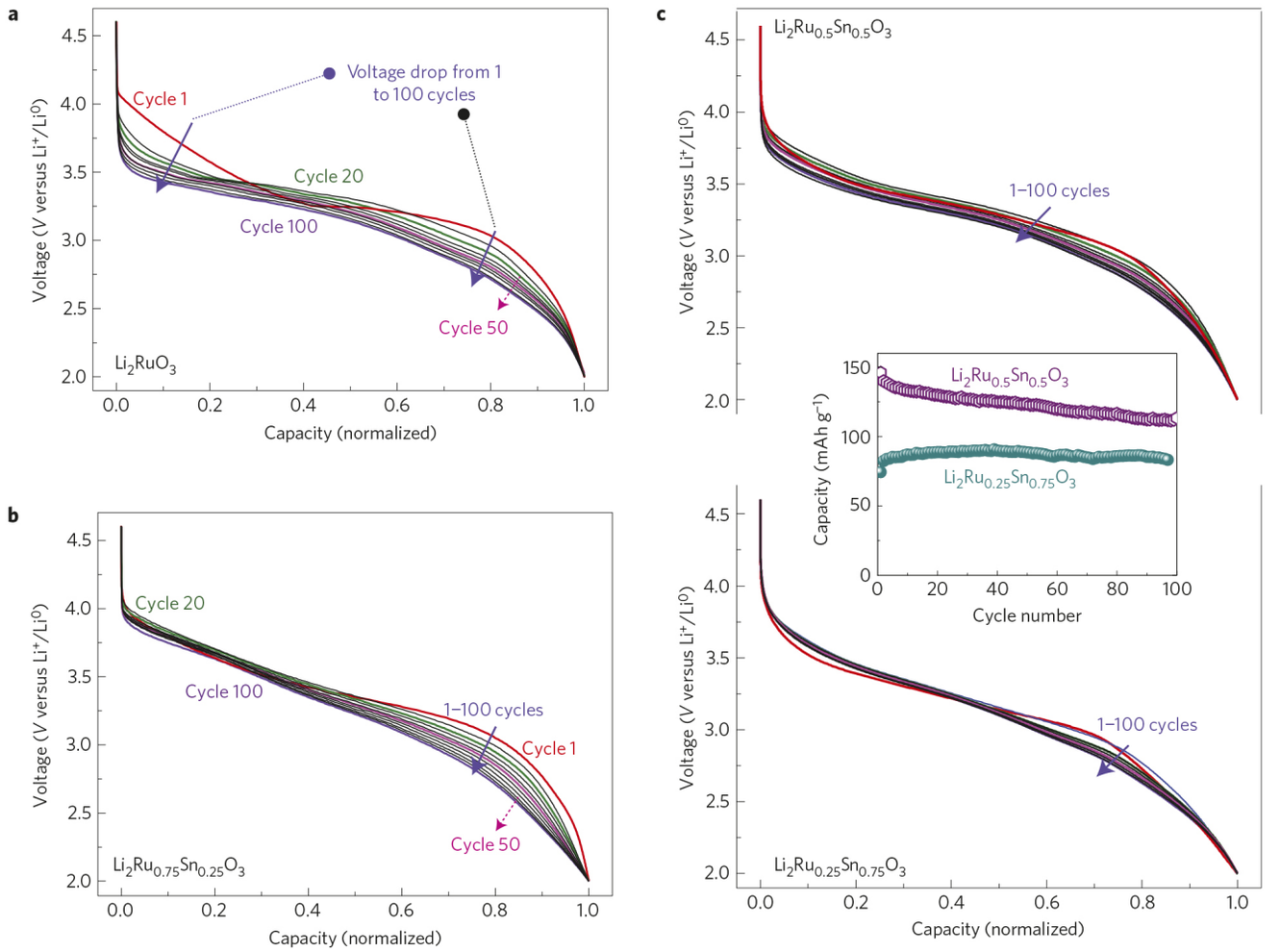

Figure 2 | Cycling behaviour of $Li_2Ru_{(1-y)}M_yO_3$ (M = Ru/Sn/Ti) in the view towards voltage decay. a–c, Normalized capacity discharge profiles for Li_2RuO_3 (**a**), $Li_2Ru_{0.75}Sn_{0.25}O_3$ (**b**), $Li_2Ru_{0.5}Sn_{0.5}O_3$ and $Li_2Ru_{0.25}Sn_{0.75}O_3$ (**c**) from 1 to 100 cycles; the data are reported only for every 10 cycle. The capacity retention for $Li_2Ru_{0.5}Sn_{0.5}O_3$ and $Li_2Ru_{0.25}Sn_{0.75}O_3$ samples is shown as an inset in **c**. The capacity normalization was performed by taking the maximum discharge capacity in the corresponding cycle as unity.

decay occurs mainly over the low potential region as confirmed by derivative curves (Fig. 1d inset), which show a progressive dumping of high to low voltage peak. When comparing the different M-based (M = Ti, Sn, Ru) samples, the voltage decay on cycling mirrors the capacity decay and is the smallest (~150 mV after 100 cycles) for $Li_2Ru_{0.75}Sn_{0.25}O_3$ (Fig. 2b). Such a trend persists whatever the amount of substituent (y; Supplementary Fig. 6). Note that the voltage decay is gradually reduced with increasing amounts of Sn in $Li_2Ru_{1-y}Sn_yO_3$ (Fig. 2a–c) with almost no voltage fading observed after 100 cycles and nearly 100% capacity retention for $y = 0.75$ (Fig. 2c inset). This clearly confirms the positive role played by larger Sn^{4+} ions in reducing the voltage decay over many cycles.

Cycling tests were also done as a function of charge cutoff voltage (Supplementary Figs 7 and 8). When cycling is limited to the Ru^{4+}/Ru^{5+} redox couple (<4 V) 100% capacity retention is observed for all systems, whereas the associated voltage decays vary from nearly zero for Sn to 80 mV for Ti. This suggests that capacity and voltage decay are not systematically related, as it may appear by raising the charge cutoff voltage to 4.2 V and 4.6 V where we note that both the capacity and voltage decay decrease in a similar manner on cycling.

In situ XRD patterns were collected at different states of charge/discharge for the $Li/Li_2Ru_{0.75}Ti_{0.25}O_3$ cell cycled at C/20 rate (Fig. 3a). As the cell is being charged to 4 V, an anisotropic variation of the lattice parameters is observed with c/a ratio decreasing from 4.99 to 4.92 suggesting a gradual suppression of Li_3–LiM_2 interlayer ordering. When further charging the cell to 4.6 V, many Bragg peaks broaden and experience changes in relative intensities, indicative of a possible migration of Ru/Ti from LiM_2 to Li_3 layers. On subsequent discharge, the structure nearly converts back to the pristine layered ordered structure with however an increasing cation disorder within the LiM_2 layers as deduced from the reduction in intensity of superstructure peaks arising from the honeycomb LiM_2 pattern.

To assess structural changes on prolonged cycling, high-resolution synchrotron powder diffraction patterns were collected for the pristine $Li_2Ru_{0.75}Ti_{0.25}O_3$ and for electrodes recovered in the discharged state after 1 and 50 cycles, respectively (Fig. 3b). After 50 cycles, the XRD pattern significantly differs from that of the first cycle by an intense peak broadening and a progressive disappearance of the superstructure peaks. Owing to such broadening, the patterns were refined in the $R\bar{3}m$ subcell using an $X^* \tan\theta$ dependence accounting for strain effects; we observed a sharp increase of the strain broadening parameter X with increasing cycle numbers (Fig. 3c). Interestingly, the XRD pattern of the $Li_2Ru_{0.75}Sn_{0.25}O_3$ electrode cycled in similar conditions (C/10 rate, cycle numbers 1, 20, 50 and 100) shows a constant X parameter (Fig. 3d), suggesting a correlation between the voltage decay and micro-strains induced by local disorder (cation migration and/or stacking fault).

XPS analyses were carried out on pristine $Li_2Ru_{0.75}Ti_{0.25}O_3$ (Fig. 4a) and on similar electrodes charged to ~3.9 V (Fig. 4b) and 4.6 V (Fig. 4c), and charge discharged to 2 V (Fig. 4d). The

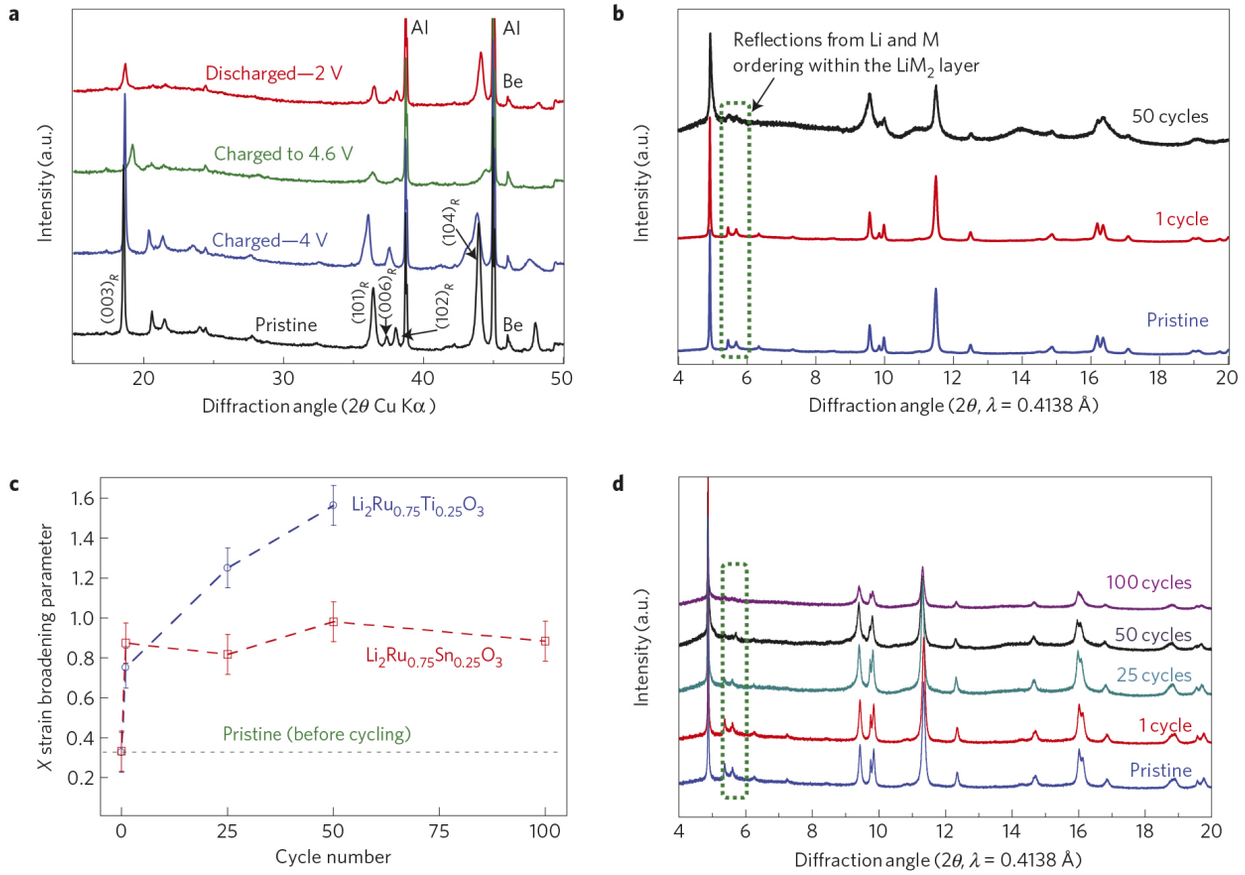

Figure 3 | Li-driven structural changes of $Li_2Ru_{0.75}M_{0.25}O_3$ (M = Sn/Ti). a, *In situ* XRD pattern of $Li_2Ru_{0.75}Ti_{0.25}O_3$ versus Li cells; the patterns collected on pristine electrode, during charge at 4 V, 4.6 V and then on completely discharged sample (2 V). On charging the Li/$Li_{2-x}Ru_{0.75}Ti_{0.25}O_3$ cell to 4 V, there is a shift in the $(003)_R$ peak towards higher 2θ and merging of $(006)_R$ and $(102)_R$ Bragg peaks (indexed in $R\bar{3}m$) indicating an anisotropic variation of lattice parameters with the removal of lithium. On discharge, most of the peaks regained their intensity and reappearance of $(006)_R$ and $(102)_R$ peak splitting shows that the structure converts back to the pristine layered ordered structure. **b**, Synchrotron powder XRD pattern of pristine $Li_2Ru_{0.75}Ti_{0.25}O_3$ and samples collected at the discharged state (2 V) after 1 cycle and 50 cycles. **c**, Variation of the Lorentzian broadening parameter $X^* \tan\theta$ with cycling derived from refinement of the synchrotron XRD patterns. **d**, Synchrotron powder XRD pattern of pristine $Li_2Ru_{0.75}Sn_{0.25}O_3$ and samples cycled several times (1, 25, 50 and 100 cycles) between 4.6 and 2 V and collected at 2 V. The green region in **b** and **c** shows the reflections from honeycomb Li–M ordering within the LiM_2 layers.

evolution of Ru $3d_{5/2}$ and O 1*s* core spectra along charge/discharge is very similar to what was previously observed in Sn-based electrodes[22]. The shift to higher binding energy of the Ru $3d_{5/2}$ core peak on moving from OCV to 4 V identifies the $Ru^{4+} \rightarrow Ru^{5+}$ oxidation process[29] (Fig. 4, left), while the appearance of the 530.4-eV O 1*s* component at higher voltages is characteristic of the formation of peroxo-like O_2^{2-} species[30]. A peculiarity here is the appearance of an O_2^{2-} peak in the 4 V sample before complete oxidation of Ru^{4+}–Ru^{5+}, for reasons to be discussed later (Supplementary Fig. 9). Repeated discharge–charge (Supplementary Fig. 10) demonstrates the reversibility of these $Ru^{4+} \rightleftharpoons Ru^{5+}$ and O^{2-}/O_2^{2-} processes, the latter being also confirmed by parallel EPR measurements (Supplementary Fig. 11) as previously described for the $Li_2Ru_{1-y}Sn_yO_3$ phases[12].

The true novelty here comes from the evolution of Ti $2p_{3/2}$ core spectra. In the pristine electrode, the Ti $2p_{3/2}$ component observed at 458.0 eV and the binding energy difference (O 1*s*–Ti $2p_{3/2}$) of 71.5 eV are characteristic of Ti^{4+} ions in an octahedral environment[31]. For samples charged to 3.9 V a small shoulder appears at 459.1 eV, which becomes prominent at 4.6 V. Such a high binding energy (that is, decrease in electron density) is characteristic of Ti^{4+} in a tetrahedral environment as reported earlier[32] and can be explained by weaker Ti $3d$–O $2p$ overlap in the tetrahedral environment. The amount of tetrahedral Ti^{4+}, as deduced from integration of the spectra, is ~15% and ~30% for the 3.9 V and 4.6 V samples, respectively. This result is consistent with the relative ease of Ti^{4+} ions migrating from octahedral to tetrahedral coordination due to the absence of ligand field stabilization[25,33]. At this point, it is tempting to suspect a correlation between the formation of O_2^{2-} entities and the Ti^{4+} migration, but such a correlation cannot be ascertained owing to the large contamination by surface oxide species that render the spectral deconvolution speculative given the small amount of O_2^{2-}. After discharge, there is appearance of an additional component at 457.2 eV which can be attributed to Ti^{3+} ions (reduction of Ti^{4+}). From quantitative analysis we could deduce that the amount of Ti^{3+} is about 35% and that octahedral Ti^{4+} ions are mainly involved in the reduction process. The spectra obtained after 30 and 50 cycles clearly indicate an increase in the amount of tetrahedral titanium from ~25% after the first cycle to ~40% after 50 cycles. Those values are further refined by the investigation of Ti 3*p* core peaks (Supplementary Fig. 12), which offer less surface sensitivity, indicating a similar evolution over many cycles with slightly lower amounts of titanium in tetrahedral sites (1 cycle: ~20%, 50 cycles: ~34%). Unfortunately, a similar approach is not feasible with Ru $3d$ because of the less resolved core spectra associated with the $Ru^{4+} \rightarrow Ru^{5+}$ oxidation process. Last, the invariance of Sn $3d$ core spectra when charging/discharging $Li_2Ru_{1-y}Sn_yO_3$ implies the absence of Sn^{4+} migration to tetrahedral interstices[12].

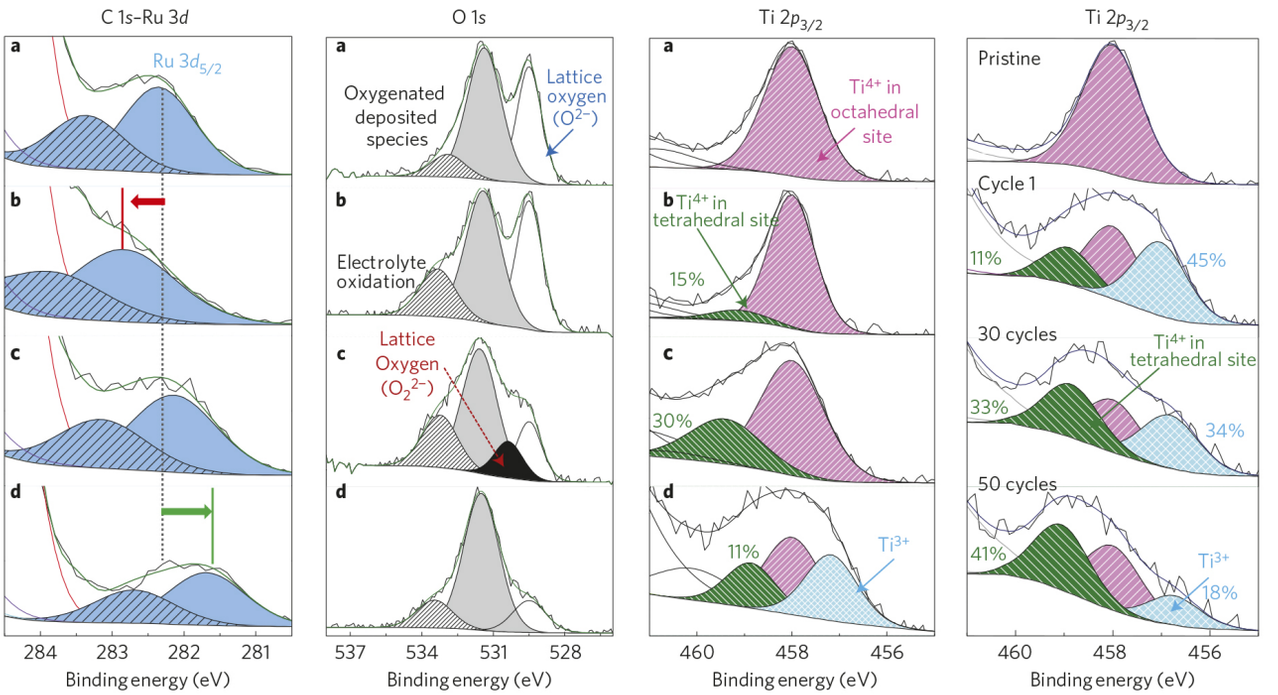

Figure 4 | XPS of $Li_2Ru_{0.75}Ti_{0.25}O_3$. a–d, XPS spectra of the pristine $Li_2Ru_{0.75}Ti_{0.25}O_3$ sample (a), 3.9 V (b), sample charged to 4.6 V (c) and charge discharged to 2 V (d). C 1s–Ru 3*d* spectra showing the Ru $3d_{5/2}$ peak (blue region) together with a satellite peak (dashed blue region). The red and green arrows and lines are guides to the eye to show the shifting of the Ru $3d_{5/2}$ peak with charging and discharging. The O 1s core spectrum consists of two peaks corresponding to crystalline O^{2-} (529.5 eV) and surface oxidized species (531.6 eV). The new component appearing at 530.5 eV for the sample charged to 4.6 V is due to peroxo-like species associated with anion contribution for the redox process. Ti $2p_{3/2}$ spectra, as a function of the cell voltage, are shown in the second panel from the right to highlight the partial migration of Ti^{4+} from the octahedral site together with its partial reduction on discharge. The right panel shows the evolution of the Ti $2p_{3/2}$ spectra with increasing number of cycles (1, 30 and 50 cycles).

Overall, XPS results show: that the Li-uptake/removal process in $Li_2Ru_{1-y}Ti_yO_3$ involves cumulative contributions of cationic ($Ti^{4+} \rightarrow Ti^{3+}/Ru^{5+} \rightarrow Ru^{4+}$) and anionic ($O_2^{2-} \rightarrow O^{2-}$) reversible redox processes; and a significant amount of Ti^{4+} migration from octahedral to tetrahedral interstices that increases on cycling (Fig. 4, right). To address the preferentially reduced Ti^{4+} sites, EPR was performed on the $Li_2Ru_{0.75}Sn_{0.25}O_3$ electrode, discharged to 2 V. The 4.2 K EPR spectrum (Supplementary Fig. 11) shows a set of two signals, with a weak g anisotropy ($g = 1.92$ and 1.89) for the first one and a lower g factor (1.79) for the second, which we ascribe to octahedral and tetrahedral Ti^{3+} centres, respectively[34,35]. This result confirms the Ti^{4+}/Ti^{3+} reduction process detected by XPS, and provides evidence for the feasibility to partially reduce Ti^{4+} in both tetrahedral and octahedral sites, although quantification could not be done.

Another feature that cannot be deduced by XPS is the degree of cation migration between octahedral sites within the LiM_2 layers and the Li_3 layers, hereafter denoted as Oc_M and Oc_{Li}, respectively, owing to nearly identical binding energies of both environments. The most natural technique to visualize cation migration at the local scale is HAADF-STEM. Thus, HAADF-STEM images were collected for the $Li_2Ru_{0.75}M_{0.25}O_3$ (M = Ti, Sn, Ru) electrodes cycled in similar conditions for various states of charge and discharge. Details on interpretation of the HAADF-STEM images are provided in Supplementary Figs 13 and 14.

We first studied the pristine $Li_2Ru_{0.75}M_{0.25}O_3$ material for which HAADF-STEM images revealed a two-dimensionally ordered structure with perfect Li and (Ru, Ti) ordering within the LiM_2 layers and no antisite defects between the Li_3 and LiM_2 layers (Supplementary Fig. 3). This contrasts with the overview [100] HAADF-STEM image (Fig. 5a) collected for a fully charged sample that shows the removal of Li to cause massive micro-structural changes, specifically: substantial disorder of the Li and (Ru, Ti) cations within the LiM_2 layers; migration of significant fractions of (Ru, Ti) cations from the octahedral Oc_M positions in the LiM_2 layers to the octahedral positions Oc_{Li} in the Li_3 layers; and the presence of local areas with partial occupation of the tetrahedral interstices between the LiM_2 and Li_3 layers by the (Ru, Ti) cations. These structural changes are not homogeneous throughout the sample, as highlighted by the three typical HAADF-STEM images in Fig. 5b–d. In the portion of the sample probed in Fig. 5b, Li and (Ru, Ti) ordering within the LiM_2 layers is mainly preserved, but a fraction of (Ru, Ti) cations migrate to the tetrahedral interstices and a marginal amount of cations move to the Oc_{Li} positions. In the area shown in Fig. 5c, the occupation of Oc_{Li} positions is greater, with nevertheless some (Ru, Ti) cations remaining at tetrahedral interstices. Last, the image in Fig. 5d shows a part of the sample in which a large fraction of (Ru, Ti) cations have moved to the Oc_{Li} site and virtually no M cations remain in the tetrahedral sites.

Turning to the discharged $Li_2Ru_{0.75}Ti_{0.25}O_3$ sample (Supplementary Fig. 15), the HAADF-STEM pattern nearly converges back to that of a pristine sample, implying that most of the cations migrate back to their initial positions. Nevertheless, some remaining traces of cations in tetrahedral interstices are observable at the edge of the crystallite, and also at the distances of 15–25 nm towards the crystallite core, where the image resolution is not yet deteriorated markedly by increasing the crystal thickness (Supplementary Fig. 16).

Next, we collected HAADF-STEM images of a $Li_2Ru_{0.75}Ti_{0.25}O_3$ electrode cycled 50 times. The images significantly differ from those collected after one cycle, showing an intense disorder of Li and (Ru, Ti) cations within the LiM_2 layers and migration of (Ru/Ti) atoms away from the LiM_2 planes towards neighbouring interstitial positions (Fig. 6a,c, left). Fitting of the HAADF-STEM signal profile reveals a dominance of peaks corresponding to the migration of (Ru/Ti) cations towards tetrahedral sites, with peaks reminiscent of Oc_{Li} site occupancy being barely visible. Overall it clearly indicates, in agreement with XPS results, that the occupancy of interstitial

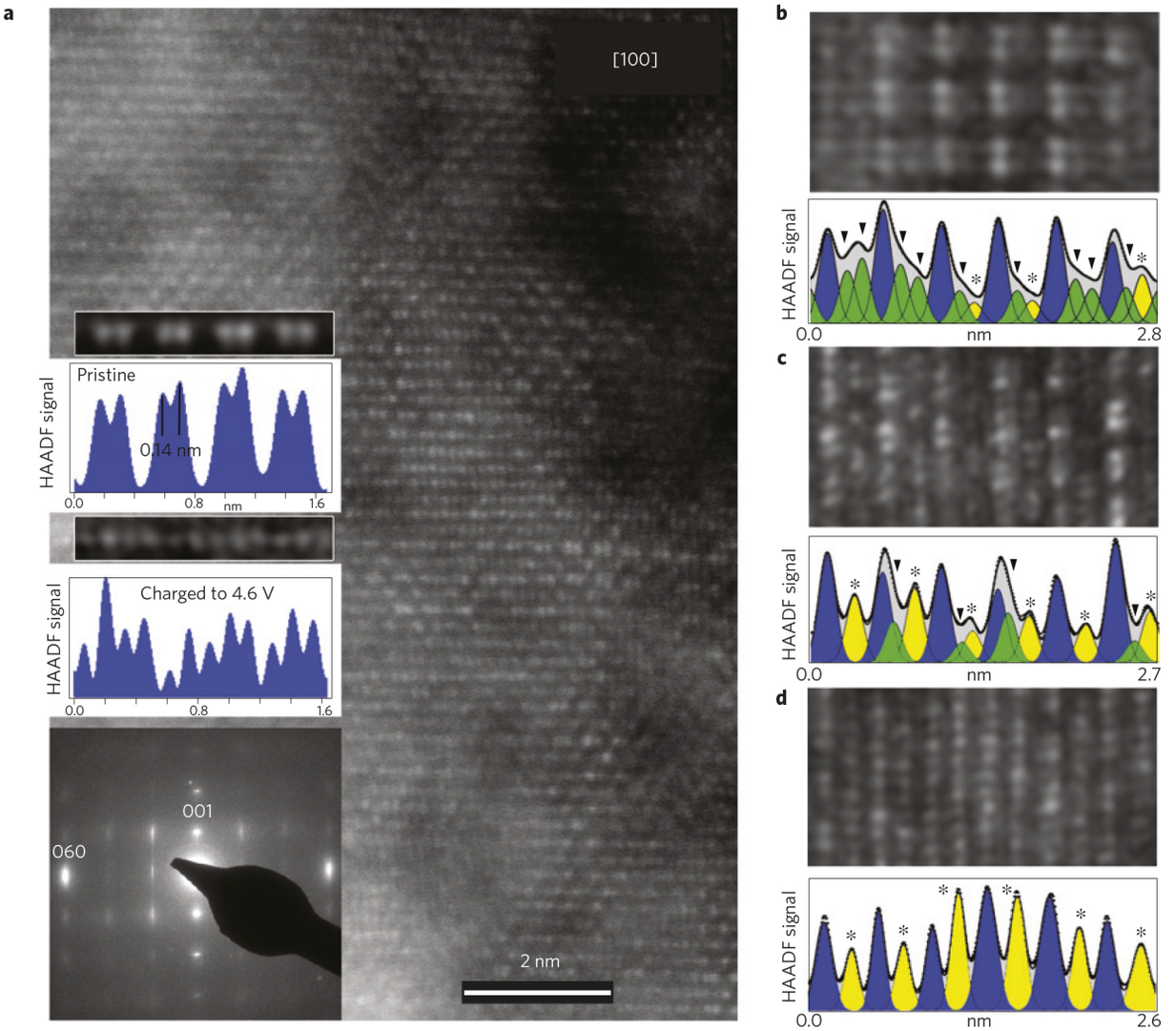

Figure 5 | HAADF-STEM images of $Li_{2-x}Ru_{0.75}Ti_{0.25}O_3$ electrodes. a, [100] overview HAADF-STEM image of the $Li_2Ru_{0.75}Ti_{0.25}O_3$ sample charged to 4.6 V. The insets show (from top to bottom): HAADF-STEM image of the atomic columns in the LiM_2 layer of the pristine $Li_2Ru_{0.75}Ti_{0.25}O_3$ sample along with the corresponding intensity profile demonstrating pair of dots separated by ~0.14 nm (this corresponds to perfect honeycomb ordering of the Li and M cations within the LiM_2 layers); HAADF-STEM image of the atomic columns in the LiM_2 layer of the charged $Li_2Ru_{0.75}Ti_{0.25}O_3$ sample along with the corresponding intensity profile demonstrating significant disorder of the M cations within the LiM_2 layers; selected-area electron diffraction pattern of the charged $Li_2Ru_{0.75}Ti_{0.25}O_3$ sample showing lines of diffuse modulated intensity at the $k \neq 3n$ positions due to local remaining order of the M cations in the LiM_2 layers. **b**–**d**, Images and corresponding HAADF-STEM signal profiles illustrating the different stages of the cation migration. **b**, The pristine structure is mostly preserved, most of the (Ru, Ti) cations are in the octahedral Oc_{LiM_2} positions (blue peaks on the profiles), but a fraction of the (Ru, Ti) cations are moved to the tetrahedral interstices (green peaks on the profile marked with arrowheads). Occupation of the octahedral positions in the Li_3 layer remains marginal (yellow peaks on the profile marked with asterisks). **c**, Occupation of the octahedral positions in the Li_3 layer increases, some (Ru, Ti) cations remain at tetrahedral interstices. **d**, A large fraction of the (Ru, Ti) cations are moved to the octahedral position in the Li_3 layer. For simplification, in the aforementioned description, the Li_3 and LiM_2 layers of the pristine structure are termed as Li_3 and LiM_2 although the cation composition of these layers is changed substantially owing to cation migration.

tetrahedral sites increases with the number of cycles. A simple explanation is that the cations are progressively trapped within the tetrahedral sites as they migrate back and forth between Oc_M and Oc_{Li} sites, suggesting a possible correlation between the voltage decay and the trapping degree on cycling.

To test such a possible correlation we explored $Li_2Ru_{0.75}Sn_{0.25}O_3$ (Fig. 6) electrodes that had been cycled 100 times and showed the lowest voltage decay. HAADF-STEM images provide direct evidence for cation migration towards Oc_{Li} sites in this system as well (Fig. 6b,c, right). More important is the quasi absence of cations in tetrahedral sites for this sample, further supporting our tentative correlation.

Finally, to clarify the outcome of Ru ions on cycling, we also studied Li_2RuO_3 electrodes cycled once, and after 100 cycles (Supplementary Figs 17 and 18). Comparing the HAADF-STEM image of Li_2RuO_3 and $Li_2Ru_{0.75}Ti_{0.25}O_3$ electrodes after one charge–discharge cycle (Supplementary Figs 16 and 17) reveals virtually no population of tetrahedral sites in the pure Ru sample. This contrasts with the HAADF-STEM images collected after 100 cycles, which indicate the presence of Ru in tetrahedral sites. However, a comparison of the HAADF-STEM signal profiles of $Li_2Ru_{0.75}Ti_{0.25}O_3$ and Li_2RuO_3 samples cycled 50 and 100 times, respectively (Fig. 6c and Supplementary Fig. 18), demonstrates that even after twice as many cycles the population of tetrahedral interstices in Li_2RuO_3 does not reach the level of $Li_2Ru_{0.75}Ti_{0.25}O_3$. Taking into account the lower rate of voltage decay for Li_2RuO_3 compared with Ti-doped samples, this further supports the relationship between cation trapping at the tetrahedral interstices and voltage decay.

With respect to practical application, the migration of cations within the van der Waals gap (namely M in the Li_3 layer) has

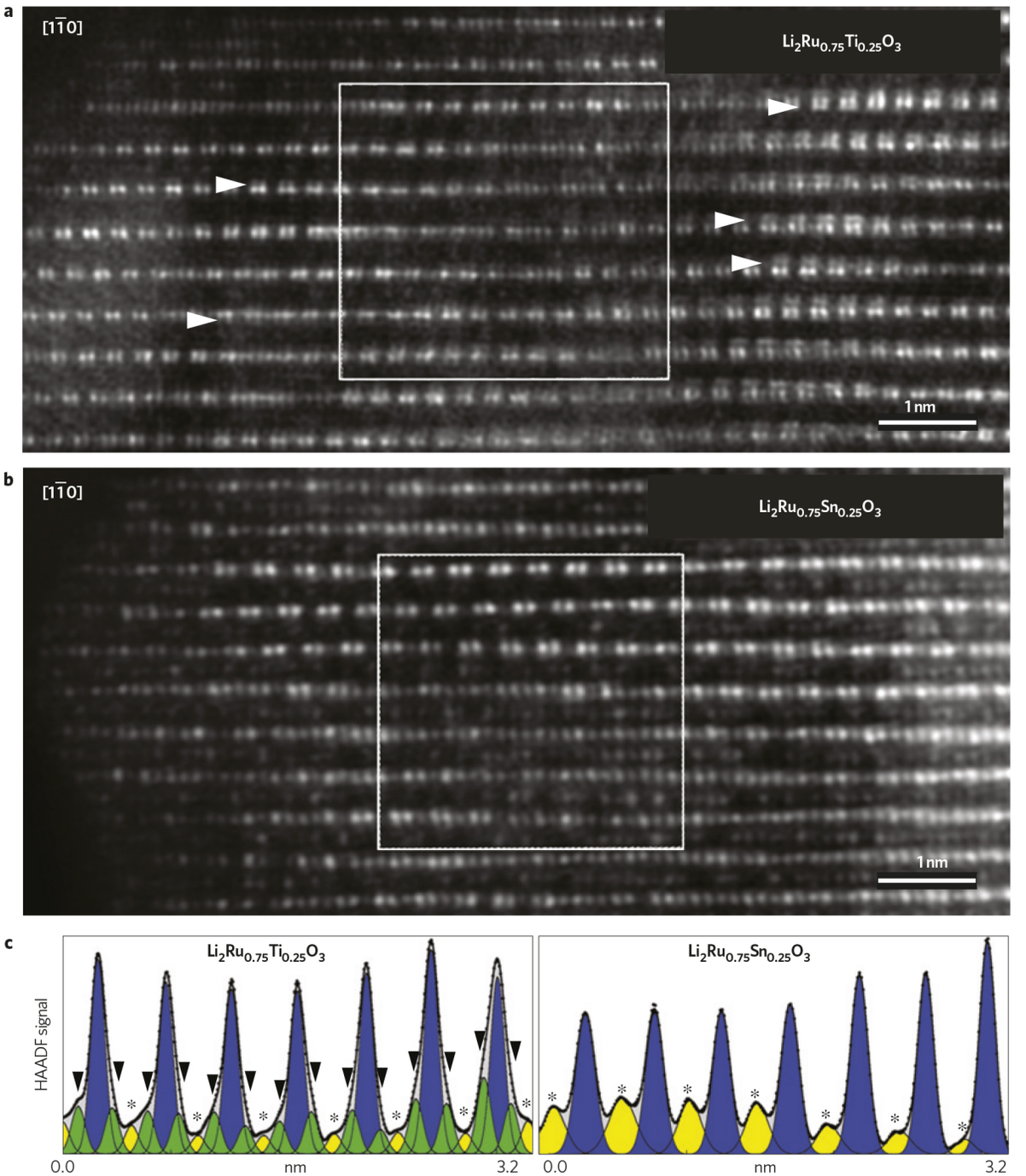

Figure 6 | Comparison of HAADF-STEM images of $Li_2Ru_{0.75}M_{0.25}O_3$ (M = Sn/ Ti) on long cycling. a, [1$\bar{1}$0] HAADF-STEM image of the $Li_2Ru_{0.75}Ti_{0.25}O_3$ sample after 50 charge–discharge cycles. Extra cations at the tetrahedral interstices next to the LiM_2 layers appear locally (some marked with arrowheads). **b**, [1$\bar{1}$0] HAADF-STEM image of the $Li_2Ru_{0.75}Sn_{0.25}O_3$ sample after 100 charge–discharge cycles. On both images the intense cation disorder is visible within the LiM_2 layers (appear brightest). Areas of the remaining order are also seen where pairs of bright dots alternate along the layers. **c**, HAADF-STEM signal profiles from areas outlined in the HAADF-STEM images. Green peaks associated with cation columns at the tetrahedral interstices are marked with arrowheads; yellow peaks of cation columns at the Oc_{Li} positions are marked with asterisks; blue peaks represent the octahedral Oc_{LiM_2} positions.

been proved to be detrimental for cycling and rate capability performances[36,37]. Here we believe that such migration is not pernicious, because it is a cooperative migration probably initiated by the formation of the peroxo-like groups that creates free space thereby opening pathways for easy in- and out-of-plane cation migration. Although the performances of such disordered systems are surprising at first, it should be recalled that numerous redox systems such as conversion or displacement reactions enlist marked structural rearrangements, and even certain amorphous compounds can also work efficiently[38–41].

Together, our studies have shown $Li_2Ru_{1-y}Ti_yO_3$ to be a model system for exploring the complex interactions between cation migration, structural rearrangements, creation of peroxo-like species and voltage decay, and reveal attractive features as discussed next in comparison with Sn-based or pure Li_2RuO_3 phases.

We found for $Li_2Ru_{1-y}Ti_yO_3$ phases an incomplete oxidation of Ru^{4+}–Ru^{5+} during the first 3.6 V plateau suggesting a competitive anionic redox process that starts at a 200–300 mV lower voltage than for the similar $Li_2Ru_{0.75}Sn_{0.25}O_3$ electrode. Lowering of potential has to be correlated with the significantly smaller volume of $Li_{2-x}Ru_{1-y}Ti_yO_3$ compared with $Li_{2-x}Ru_{1-y}Sn_yO_3$, which increases the Ru($4d$)–O($2p$) band overlap and therefore the covalent character of Ru–O bonds. Moreover, Ti and Sn substitutions, in spite of the fact that neither Sn^{4+} nor Ti^{4+} has free d electrons,

play different roles on the $Li_{2-x}Ru_yM_{1-y}O_3$ (M = Ti/Sn) band structures. Whereas the Sn(5*s*, 5*p*, 5*d*) bands are too high in energy to overlap with the O(2*p*) bands, the low-lying empty Ti(3*d*) bands allow this overlap that raises the O–O anti-bonding band (Supplementary Fig. 19). These structural and electronic features not only enable the oxidation of oxo-ligands to peroxo-like species at lower potential for the Ti-substituted samples but also limit the flexibility of the oxygen lattice, which is therefore more prone to O_2 release than for the Sn-substituted samples, as confirmed by differential electrochemical mass spectroscopy experiments (data not shown).

Collectively, these data establish a robust correlation between the voltage decay shown by Li-rich $Li_2Ru_{1-y}M_yO_3$ phases and the amount of cations that remain locked in tetrahedral sites. The largest decay was observed for Ti^{4+}, which owing to its smaller size compared with Sn^{4+}, is more prone to migrate via an intermediary tetrahedral site and hence to be trapped. Cation migration in layered oxides has been the subject of theoretical studies that have predicted several migration paths enlisting the migration of cations from Oc_{LiM_2} to Oc_{Li_3} sites either directly or via intermediary tetrahedral sites with the latter one being energetically favourable[25,42]. Therefore, we decided to revisit such calculations which because it was not known at that time were done without considering the reversible formation of a peroxo-like group in these Li-rich compounds.

Density functional theory (DFT) calculations performed on the present $Li_1Ru_{1/2}M_{1/2}O_3$ (M = Ru, Ti, Sn) compounds (see Table in Supplementary Fig. 20) confirm that Ti^{4+} is the only cation stable in a tetrahedral coordination at this Li composition. More interestingly, the $LiRu_{0.5}Ti_{0.5}O_3$ relaxed structure shows a spontaneous migration of Ti^{4+} cations from Oc_{LiM_2} to Td_{LiM_2}, concomitantly with the formation of peroxo-like groups (Supplementary Fig. 20b) whereas the Sn^{4+} ions in $LiRu_{0.5}Sn_{0.5}O_3$ remain in their Oc_{LiM_2} sites in accordance with our experimental findings. In contrast, for pure $LiRuO_3$ the Ru^{5+} spontaneously migrates from Td_{Li_3} or Td_{LiM_2} to Oc_{Li_3}, the latter showing equivalent thermodynamic stability to Oc_{LiM_2} (to 23 meV). This suggests a low kinetic barrier for the $Oc_{LiM_2} \rightarrow Oc_{LiM_2} \rightarrow Oc_{LiM_2}$ path in this system, perfectly consistent with the enlarged migration pathway resulting from the formation of peroxo-like species (Supplementary Fig. 20c). For the fully charged material RuO_3, we note that the tetrahedral sites become more favourable than the Oc_{Li_3} and as favourable as the Oc_{LiM_2}, in perfect agreement with our microscopy results showing some Ru in tetrahedral sites after long cycling (see Table in Supplementary Figs 20 and 21).

In summary, we show that cation migration is an intrinsic and inseparable part of the charge–discharge process in the Li-rich phases and also that the continuous reduction in the averaged cell voltage is nested in the trapping of metal ions in tetrahedral sites that seem to favour the stability of delithiated structures. Although no straightforward solution yet exists, this study suggests research directions that may help obviate the voltage decay issue. One route is to increase the amount of large spectator ions, such as tin, to slow down or prevent the Td trapping. Tin's beneficial effect is demonstrated by a 50% decrease in voltage fading when increasing the amount of Sn from 25% to 50% (Fig. 2b,c), but this is at the expense of an energy density penalty rendering this approach poorly attractive. An alternative is the use of electro-active cations larger than Ru while ensuring strong *d*–*sp* hybridization to take advantage of the additional $O^{2-} \rightarrow O_2^{2-}$ redox capacity. This can be realized by moving to 4*d* metals such as Mo or Nb. Recent work on new cation-disordered rock-salt phases $Li_{1.3}Nb_{1-x}M_xO_2$ (ref. 43) having capacities approaching 300 mAh g^{-1} validates our reasoning although the long-term cycling of such phases is not yet reported. We hope this better understanding of the voltage decay phenomenon will provide clues to chemists for identifying formulations to harvest all advantages of this new class of high-capacity electrodes based on dual cationic and anionic redox mechanisms.

Methods

Synthesis of $Li_2Ru_{1-y}Ti_yO_3$ ($0 \le y \le 1$). Stoichiometric amounts of RuO_2 (Sigma-Aldrich 99.9%) and TiO_2 (Sigma-Aldrich 98%) were homogenized, using a mortar and pestle for 20 min and then ball milled for 40 min with a 10 wt% excess of Li_2CO_3 (Sigma-Aldrich, purity 99.0%) to compensate its volatilization at high temperature. The resultant mixture was heated at 800 °C for 24 h with intermediate grinding. Furnace heating and cooling rate was maintained at 2 °C min^{-1}.

XRD. XRD patterns were recorded using a Bruker D8 diffractometer equipped with a Cu Kα radiation source ($\lambda_1 = 1.54056$ Å, $\lambda_2 = 1.54439$ Å) and a LynxEye detector operated at 40 kV and 40 mA. The powder XRD patterns were refined using the Rietveld method[44] as implemented in the FullProf program[45]. *In situ* XRD analysis was carried out in a specially made Swagelok-type stainless-steel cell with an X-ray-transparent Be window. An aluminium foil was used between the Be window and the active material to prevent the oxidation of Be at higher operating voltages. High-resolution synchrotron powder diffraction patterns were collected on powders sealed under argon in glass capillaries of 0.8 mm diameter. The data were collected at the 11-BM beamline through the mail-in program at the Advanced Photon Source, ANL using a beam of wavelength 0.41 Å.

Electrochemical insertion/extraction of Li^+. Electrochemical tests versus Li were done in Swagelok-type cells. The cells were assembled in an argon-filled glove box, using a ball-milled mixture of pristine material ($Li_2Ru_{(1-y)}M_yO_3$, M = Ti/Sn/Ru) with 10% of SP carbon as the positive electrode and a Li metal disc as the negative electrode. A Whatman GF/D borosilicate glass fibre sheet separator saturated with 1 M $LiPF_6$ solution in a mixture of ethylene carbonate, propylene carbonate and dimethyl carbonate in a 1:1:3 ratio by weight (LP100) was employed. The mechanical mixing was performed under an argon atmosphere using a Spex-800 mixer-mill. Galvanostatic charge–discharge tests were conducted at 20 °C using a Mac-Pile or a VMP system (Biologic S.A.) operating in galvanostatic mode. Unless otherwise specified, the cells were typically cycled between 4.6 and 2 V versus Li^+/Li^0 at 1 Li^+ exchanged per 5 h (C/5). All of the results reported herein have been reproduced at least twice.

XPS data collection and analysis. XPS measurements were carried out using a Kratos Axis Ultra spectrometer connected through a transfer chamber to an argon-filled dry box. The samples were carefully transferred to the XPS spectrometer without any exposure to air/moisture and were analysed using monochromatized Al Kα radiation (1,486.6 eV). The pressure in the analysis chamber was maintained at around 5×10^{-9} mbar. Short acquisition time spectra were recorded before each experiment to analyse the stability of the sample under irradiation and then the normal spectra were collected with a constant pass energy of 20 eV. The binding energy scale was calibrated using the C 1*s* peak at 285.0 eV and the peak positions and areas were optimized by a weighted least-squares fitting method using 70% Gaussian, 30% Lorentzian line shapes. Quantification was performed on the basis of Scofield's relative sensitivity factors.

EPR spectra. EPR spectra were recorded using a Brüker ELEXSYS E580 spectrometer at 5 mW microwave power and 5G modulation amplitude. The measurements were carried out at room temperature and at 4 K.

Transmission electron microscopy. The samples were handled in an Ar-filled glove box. TEM specimens were prepared in the glove box by crushing the crystals in a mortar in anhydrous hexane and depositing drops of suspension onto holey carbon grids. The specimens were transported to the microscope column completely excluding contact with air. Electron diffraction patterns were obtained with a Tecnai G^2 electron microscope operated at 200 kV. HAADF-STEM images were obtained with aberration-corrected Titan G^3 electron microscopes operated at 200 kV using a convergence semi-angle of 21.6 mrad. The HAADF inner collection semi-angle was 70 mrad.

DFT + *U* calculations. Spin-polarized DFT + *U* ($U_{eff} = 4$ eV for Ru) calculations were performed using the VASP code[46,47] and the GGA-PBE functional[48]. The plane-wave energy cutoff was set to 600 eV and the Brillouin zone integration was done in a *k*-point grid distributed as uniformly as possible. All atom coordinates and lattice parameters were fully relaxed using conjugate gradient energy minimization until the forces acting on each atom were less than 5×10^{-3} eV $Å^{-2}$.

References

1. Whittingham, M. S. Materials challenges facing electrical energy storage. *MRS Bull.* **33,** 411–419 (2008).
2. Armand, M. & Tarascon, J-M. Building better batteries. *Nature* **451,** 652–657 (2008).
3. Palacin, M. R. Recent advances in rechargeable battery materials: A chemist's perspective. *Chem. Soc. Rev.* **38,** 2565–2575 (2009).
4. Armand, M. & Tarascon, J-M. Issues and challenges facing rechargeable lithium batteries. *Nature* **414,** 359–367 (2001).
5. Prosini, P. P. *Iron Phosphate Materials as Cathodes for Lithium Batteries* (Springer, 2011).
6. Rousse, G. & Tarascon, J-M. Sulfate-based polyanionic compounds for Li-ion batteries: Synthesis, crystal chemistry, and electrochemistry aspects. *Chem. Mater.* http://dx.doi.org/10.1021/cm4022358 (2013).
7. He, P., Yu, H., Li, D. & Zhou, H. Layered lithium transition metal oxide cathodes towards high energy lithium-ion batteries. *J. Mater. Chem.* **22,** 3680–3695 (2012).
8. Ohzuku, T. & Makimura, Y. Layered lithium insertion material of $LiCo_{1/3}Ni_{1/3}Mn_{1/3}O_2$ for lithium-ion batteries. *Chem. Lett.* **30,** 642–643 (2001).
9. Koyama, Y., Tanaka, I., Adachi, H., Makimura, Y. & Ohzuku, T. Crystal and electronic structures of superstructural $Li_{1-x}[Co_{1/3}Ni_{1/3}Mn_{1/3}]O_2$ ($0 \le x \le 1$). *J. Power Sources* **119–121,** 644–648 (2003).
10. Thackeray, M. M. *et al.* Li_2MnO_3-stabilized $LiMO_2$ (M = Mn, Ni, Co) electrodes for lithium-ion batteries. *J. Mater. Chem.* **17,** 3112–3125 (2007).
11. Zhou, F., Zhao, X., van Bommel, A., Xia, X. & Dahn, J. R. Comparison of $Li[Li_{1/9}Ni_{1/3}Mn_{5/9}]O_2$, $Li[Li_{1/5}Ni_{1/5}Mn_{3/5}]O_2$, $LiNi_{0.5}Mn_{1.5}O_4$, and $LiNi_{2/3}Mn_{1/3}O_2$ as high voltage positive electrode materials. *J. Electrochem. Soc.* **158,** A187–A191 (2011).
12. Sathiya, M. *et al.* Reversible anionic redox chemistry in high-capacity layered-oxide electrodes. *Nature Mater.* **12,** 827–835 (2013).
13. Koga, H. *et al.* Reversible oxygen participation to the redox processes revealed for $Li_{1.20}Mn_{0.54}Co_{0.13}Ni_{0.13}O_2$. *J. Electrochem. Soc.* **160,** A786–A792 (2013).
14. Bettge, M. *et al.* Voltage fade of layered oxides: Its measurement and impact on energy density. *J. Electrochem. Soc.* **160,** A2046–A2055 (2013).
15. Gallagher, K. G. *et al.* Correlating hysteresis and voltage fade in lithium- and manganese-rich layered transition-metal oxide electrodes. *Electrochem. Commun.* **33,** 96–98 (2013).
16. Croy, J. R. *et al.* Examining hysteresis in composite $xLi_2MnO_3 \cdot (1-x)LiMO_2$ cathode structures. *J. Phys. Chem. C* **117,** 6525–6536 (2013).
17. Gu, M. *et al.* Formation of the spinel phase in the layered composite cathode used in Li-ion batteries. *ACS Nano* **7,** 760–767 (2012).
18. Mohanty, D. *et al.* Investigating phase transformation in the $Li_{1.2}Co_{0.1}Mn_{0.55}Ni_{0.15}O_2$ lithium-ion battery cathode during high-voltage hold (4.5 V) via magnetic, X-ray diffraction and electron microscopy studies. *J. Mater. Chem. A* **1,** 6249–6261 (2013).
19. Ito, A. *et al.* Direct observation of the partial formation of a framework structure for Li-rich layered cathode material $Li[Ni_{0.17}Li_{0.2}Co_{0.07}Mn_{0.56}]O_2$ upon the first charge and discharge. *J. Power Sources* **196,** 4785–4790 (2011).
20. Zheng, J. *et al.* Corrosion/fragmentation of layered composite cathode and related capacity/voltage fading during cycling process. *Nano Lett.* **13,** 3824–3830 (2013).
21. Croy, J. R. *et al.* Countering the voltage decay in high capacity $xLi_2MnO_3 \cdot (1-x)LiMO_2$ electrodes (M = Mn, Ni, Co) for Li^+-ion batteries. *J. Electrochem. Soc.* **159,** A781–A790 (2012).
22. Hong, J. *et al.* Structural evolution of layered $Li_{1.2}Ni_{0.2}Mn_{0.6}O_2$ upon electrochemical cycling in a rechargeable battery. *J. Mater. Chem.* **20,** 10179–10186 (2010).
23. Xu, B., Fell, C-R., Chi, M. & Meng, Y-S. Identifying surface structural changes in layered Li-excess nickel manganese oxides in high voltage lithium ion batteries: A joint experimental and theoretical study. *Energy Environ. Sci.* **4,** 2223–2233 (2011).
24. Sathiya, M. *et al.* High performance $Li_2Ru_{1-y}Mn_yO_3$ ($0.2 \le y \le 0.8$) cathode materials for rechargeable lithium-ion batteries: Their understanding. *Chem. Mater.* **25,** 1121–1131 (2013).
25. Reed, J. & Ceder, G. Role of electronic structure in the susceptibility of metastable transition-metal oxide structures to transformation. *Chem. Rev.* **104,** 4513–4534 (2004).
26. Kang, K. & Ceder, G. Factors that affect Li mobility in layered lithium transition metal oxides. *Phys. Rev. B* **74,** 094105 (2006).
27. Yu, H. & Zhou, H. High-energy cathode materials (Li_2MnO_3–$LiMO_2$) for lithium-ion batteries. *J. Phys. Chem. Lett.* **4,** 1268–1280 (2013).
28. Kang, S. H. *et al.* Interpreting the structural and electrochemical complexity of $0.5Li_2MnO_3.0.5LiMO_2$ electrodes for lithium batteries ($M = Mn_{0.5-x}Ni_{0.5-x}Co_{2x}$, $0 \le x \le 0.5$). *J. Mater. Chem.* **17,** 2069–2077 (2007).
29. Manju, U., Awana, V. P. S., Kishan, H. & Sarma, D. D. X-ray photoelectron spectroscopy of superconducting $RuSr_2Eu_{1.5}Ce_{0.5}Cu_2O_{10}$ and nonsuperconducting $RuSr_2EuCeCu_2O_{10}$. *Phys. Rev. B* **74,** 245106 (2006).
30. Dupin, J-C., Gonbeau, D., Vinatier, P. & Levasseur, A. Systematic XPS studies of metal oxides, hydroxides and peroxides. *Phys. Chem. Chem. Phys.* **2,** 1319–1324 (2000).
31. Atuchin, V. V., Kesler, V. G., Pervukhina, N. V. & Zhang, Z. Ti 2*p* and O 1*s* core levels and chemical bonding in titanium-bearing oxides. *J. Electron Spectrosc. Relat. Phenom.* **152,** 18–24 (2006).
32. Arillo, M. A. *et al.* Surface characterisation of spinels with Ti(IV) distributed in tetrahedral and octahedral sites. *J. Alloys Compd.* **317–318,** 160–163 (2001).
33. Kang, K. *et al.* Synthesis and electrochemical properties of layered $Li_{0.9}Ni_{0.45}Ti_{0.55}O_2$. *Chem. Mater.* **15,** 4503–4507 (2003).
34. Morra, E., Giamello, E. & Chiesa, M. Probing the redox chemistry of titanium silicate-1: Formation of tetrahedral Ti^{3+} centers by reaction with triethyl aluminium. *Chemistry* **20(24),** 7381–7388 (2014).
35. Lopez, M. C. *et al.* Tunable Ti^{4+}/Ti^{3+} redox potential in the presence of iron and calcium in NASICON-type related phosphates as electrodes for lithium batteries. *Chem. Mater.* **25,** 4025–4035 (2013).
36. Lu, Z. & Dahn, J. R. *In situ* and *ex situ* XRD investigation of $Li[Cr_xLi_{1/3-x/3}Mn_{2/3-2x/3}]O_2$ ($x = 1/3$) cathode material. *J. Electrochem. Soc.* **150,** A1044–A1051 (2003).
37. Bak, S-M. *et al.* Correlating structural changes and gas evolution during the thermal decomposition of charged $Li_xNi_{0.8}Co_{0.15}Al_{0.05}O_2$ cathode materials. *Chem. Mater.* **25,** 337–351 (2013).
38. Morcrette, M. *et al.* A reversible copper extrusion-insertion electrode for rechargeable Li batteries. *Nature Mater.* **2,** 755–761 (2003).
39. Qian, J., Qiao, D., Ai, X., Cao, Y. & Yang, H. Reversible 3-Li storage reactions of amorphous phosphorus as high capacity and cycling-stable anodes for Li-ion batteries. *Chem. Commun.* **48,** 8931–8933 (2012).
40. Poizot, P. *et al.* Evidence of an electrochemically assisted ion exchange reaction in $Cu_{2.33}V_4O_{11}$ electrode material vs. Li. *Electrochem. Solid-State Lett.* **8,** A184–A187 (2005).
41. Lee, J. *et al.* Unlocking the potential of cation-disordered oxides for rechargeable lithium batteries. *Science* **343,** 519–522 (2014).
42. Reed, J., Ceder, G. & Van Der Ven, A. Layered-to-spinel phase transition in Li_xMnO_2. *Electrochem. Solid-State Lett.* **4,** A78–A81 (2001).
43. Yabuuchi, N. *et al. 224th ECS Meeting* (The Electrochemical Society, 2013).
44. Rietveld, H. M. A profile refinement method for nuclear and magnetic structures. *J. Appl. Crystallogr.* **2,** 65–71 (1969).
45. Rodriguez-Carvajal, J. Recent advances in magnetic-structure determination by neutron powder diffraction. *Physica B* **192,** 55–69 (1993).
46. Kresse, G. & Furthmüller, J. Efficiency of *ab-initio* total energy calculations for metals and semiconductors using a plane-wave basis set. *Comput. Mater. Sci.* **6,** 15–50 (1996).
47. Kresse, G. & Hafner, J. *Ab initio* molecular dynamics for liquid metals. *Phys. Rev. B* **47,** 558–561 (1993).
48. Perdew, J. P., Burke, K. & Ernzerhof, M. Generalized gradient approximation made simple. *Phys. Rev. Lett.* **77,** 3865–3868 (1996).

Acknowledgements

The authors acknowledge both ALISTORE-ERI and RS2E institutions for fully supporting this work. G.V.T. acknowledges the European Research Council, ERC grant No. 246791–COUNTATOMS. The research leading to these results has received funding from the European Union Seventh Framework Programme under Grant Agreement 312483-ESTEEM2 (Integrated Infrastructure Initiative–I3). C.P.L. thanks the CSIR, New Delhi for granting a Senior Research Fellowship. Use of the APS (Advanced Photon Source) at Argonne National Laboratory (ANL) supported by the US Department of Energy under Contract No. DE-AC02-06CH11357 is greatly acknowledged.

Author contributions

M.Sathiya, K.R., C.P.L. and A.S.P. carried out the synthesis, M.Sathiya, and J-M.T. conducted the electrochemical work and J-M.T. designed the research approach; G.R. analysed the crystal structures and diffraction patterns; A.M.A. and G.V.T. carried out, analysed and exploited the electron diffraction and HAADF-STEM studies; D.F. and D.G. collected and analysed the XPS spectra; M.Saubanère and M.L.D. conducted the DFT calculations and developed the theoretical framework; M.Sathiya, A.M.A. and J-M.T. wrote the manuscript and all authors discussed the experiments and final manuscript.

Additional information

Supplementary information is available in the online version of the paper. Reprints and permissions information is available online at www.nature.com/reprints. Correspondence and requests for materials should be addressed to J-M.T.

Competing financial interests

The authors declare no competing financial interests.